Article

The nature of an ultra-faint galaxy in the cosmic dark ages seen with JWST

https://doi.org/10.1038/s41586-023-05994-w

Received: 27 October 2022

Accepted: 21 March 2023

Published online: 17 May 2023

Check for updates

Guido Roberts-Borsani[1]✉, Tommaso Treu[1], Wenlei Chen[2], Takahiro Morishita[3], Eros Vanzella[4], Adi Zitrin[5], Pietro Bergamini[4,6], Marco Castellano[7], Adriano Fontana[7], Karl Glazebrook[8], Claudio Grillo[6,9], Patrick L. Kelly[2], Emiliano Merlin[7], Themiya Nanayakkara[8], Diego Paris[7], Piero Rosati[4,10], Lilan Yang[11], Ana Acebron[6,9], Andrea Bonchi[7,12], Kit Boyett[13,14], Maruša Bradač[15,16], Gabriel Brammer[17,18], Tom Broadhurst[19,20,21], Antonello Calabró[7], Jose M. Diego[22], Alan Dressler[23], Lukas J. Furtak[5], Alexei V. Filippenko[24], Alaina Henry[25,26], Anton M. Koekemoer[25], Nicha Leethochawalit[27], Matthew A. Malkan[1], Charlotte Mason[17,18], Amata Mercurio[28,29], Benjamin Metha[1,13,14], Laura Pentericci[7], Justin Pierel[25], Steven Rieck[2], Namrata Roy[26], Paola Santini[7], Victoria Strait[17,18], Robert Strausbaugh[30], Michele Trenti[13,14], Benedetta Vulcani[31], Lifan Wang[32], Xin Wang[33,34,35] & Rogier A. Windhorst[36]

In the first billion years after the Big Bang, sources of ultraviolet (UV) photons are believed to have ionized intergalactic hydrogen, rendering the Universe transparent to UV radiation. Galaxies brighter than the characteristic luminosity L^* (refs. 1,2) do not provide enough ionizing photons to drive this cosmic reionization. Fainter galaxies are thought to dominate the photon budget; however, they are surrounded by neutral gas that prevents the escape of the Lyman-α photons, which has been the dominant way to identify them so far. JD1 was previously identified as a triply-imaged galaxy with a magnification factor of 13 provided by the foreground cluster Abell 2744 (ref. 3), and a photometric redshift of $z \approx 10$. Here we report the spectroscopic confirmation of this very low luminosity ($\approx 0.05\,L^*$) galaxy at $z = 9.79$, observed 480 Myr after the Big Bang, by means of the identification of the Lyman break and redward continuum, as well as multiple $\gtrsim 4\sigma$ emission lines, with the Near-InfraRed Spectrograph (NIRSpec) and Near-InfraRed Camera (NIRCam) instruments. The combination of the James Webb Space Telescope (JWST) and gravitational lensing shows that this ultra-faint galaxy ($M_{\mathrm{UV}} = -17.35$)—with a luminosity typical of the sources responsible for cosmic reionization—has a compact (≈150 pc) and complex morphology, low stellar mass ($10^{7.19}\,M_{\odot}$) and subsolar ($\approx 0.6\,Z_{\odot}$) gas-phase metallicity.

The galaxy JD1 was observed by the James Webb Space Telescope (JWST) with deep Near-InfraRed Camera (NIRCam) imaging (general observer programme 2561; principal investigator (PI), Labbé, and director's discretionary time (DDT) programme 2756; PI Chen) and Near-InfraRed Spectrograph (NIRSpec) prism spectroscopy (DDT programme 2756; PI Chen). Residing behind the Abell 2744 galaxy cluster, the source is gravitationally lensed and displays three images, of which two bright components (A and B) reside to the north of the main galaxy cluster and a fainter component (C) to the south. The NIRCam images cover all three components, whereas NIRSpec prism spectroscopy targeted the brightest component (component B; spectral overlap prevented us from observing both) on 23 October 2022. An RGB image using the

[1]Department of Physics and Astronomy, University of California, Los Angeles, CA, USA. [2]School of Physics and Astronomy, University of Minnesota, Minneapolis, MN, USA. [3]Infrared Processing and Analysis Center, Caltech, Pasadena, CA, USA. [4]INAF - OAS, Osservatorio di Astrofisica e Scienza dello Spazio di Bologna, Bologna, Italy. [5]Physics Department, Ben-Gurion University of the Negev, Be'er-Sheva, Israel. [6]Dipartimento di Fisica, Università degli Studi di Milano, Milan, Italy. [7]INAF Osservatorio Astronomico di Roma, Monteporzio Catone, Rome, Italy. [8]Centre for Astrophysics and Supercomputing, Swinburne University of Technology, Hawthorn, Victoria, Australia. [9]INAF - IASF Milano, Milan, Italy. [10]Dipartimento di Fisica e Scienze della Terra, Università degli Studi di Ferrara, Ferrara, Italy. [11]Kavli Institute for the Physics and Mathematics of the Universe, The University of Tokyo, Kashiwa, Japan. [12]ASI-Space Science Data Center, Rome, Italy. [13]School of Physics, University of Melbourne, Parkville, Victoria, Australia. [14]ARC Centre of Excellence for All Sky Astrophysics in 3 Dimensions (ASTRO 3D), Canberra, Australian Capital Territory, Australia. [15]University of Ljubljana, Department of Mathematics and Physics, Ljubljana, Slovenia. [16]Department of Physics and Astronomy, University of California, Davis, CA, USA. [17]Cosmic Dawn Center (DAWN), Copenhagen, Denmark. [18]Niels Bohr Institute, University of Copenhagen, Copenhagen, Denmark. [19]Department of Theoretical Physics, University of the Basque Country UPV/EHU, Bilbao, Spain. [20]Donostia International Physics Center (DIPC), Donostia, Spain. [21]IKERBASQUE, Basque Foundation for Science, Bilbao, Spain. [22]Instituto de Física de Cantabria (CSIC-UC), Santander, Spain. [23]The Observatories, The Carnegie Institution for Science, Pasadena, CA, USA. [24]Department of Astronomy, University of California, Berkeley, CA, USA. [25]Space Telescope Science Institute, Baltimore, MD, USA. [26]Center for Astrophysical Sciences, Department of Physics & Astronomy, Johns Hopkins University, Baltimore, MD, USA. [27]National Astronomical Research Institute of Thailand (NARIT), Mae Rim, Thailand. [28]Dipartimento di Fisica 'E.R. Caianiello', Università degli Studi di Salerno, Fisciano (SA), Italy. [29]INAF-Osservatorio Astronomico di Capodimonte, Naples, Italy. [30]Minnesota Institute For Astrophysics, University of Minnesota, Minneapolis, MN, USA. [31]INAF Osservatorio Astronomico di Padova, Padova, Italy. [32]Mitchell Institute for Fundamental Physics & Astronomy, Texas A&M University, Department of Physics and Astronomy, College Station, TX, USA. [33]School of Astronomy and Space Science, University of Chinese Academy of Sciences (UCAS), Beijing, China. [34]National Astronomical Observatories, Chinese Academy of Sciences, Beijing, China. [35]Institute for Frontiers in Astronomy and Astrophysics, Beijing Normal University, Beijing, China. [36]School of Earth and Space Exploration, Arizona State University, Tempe, AZ, USA. ✉e-mail: guidorb@astro.ucla.edu

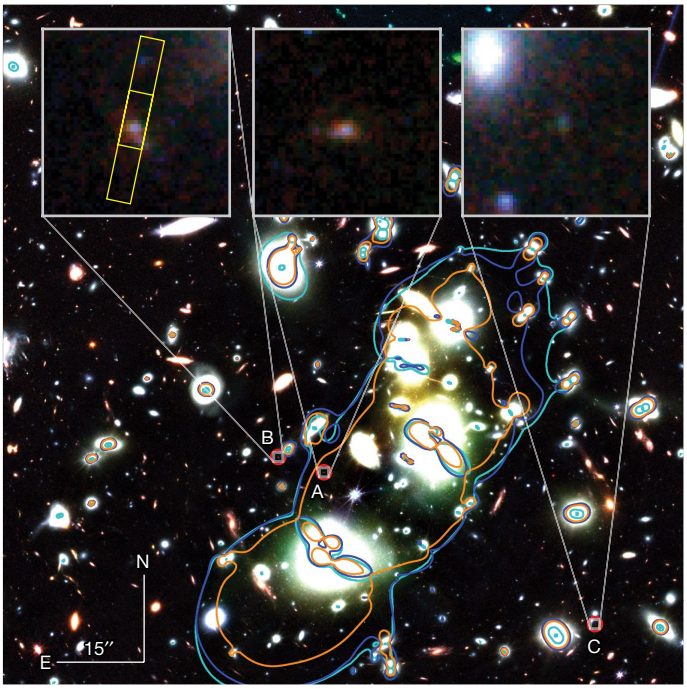

Fig. 1 | A false-colour NIRCam image of the Abell 2744 cluster. Critical curves of formally infinite magnification from two lensing models (Bergamini et al.[5] (in blue) and an update to Zitrin et al.[3] (in cyan), discussed in the Methods section) are plotted . The A, B and C multiple images of the $z = 9.79$ galaxy are highlighted by red circles. The inset plots represent zoom-ins on each of the triply-imaged components, with the brightest component (JD1) highlighted by the 0. 2″ × 1. 2″ NIRSpec slit (constructed using three MSA shutters) used for prism spectroscopy in our DDT programme. Critical lines for a source at $z \approx 10$, the redshift indicated by the lens model, the photometry and the spectroscopy, are in excellent mutual agreement—highlighting the robustness of the lens model—and fall between the two images consistent with their similar brightness. To show the power of lensing to constrain the redshift of the source, we also show, as an orange line, the critical line for a source at $z = 2.24$ (ref. 5). If JD1 were at this lower redshift, the image positions and fluxes would be inconsistent with the measurements. Here B = F115W + F150W, G = F200W + F277W and R = F356W + F444W.

novel NIRCam data is shown in Fig. 1, where we highlight a portion of the cluster field (including the positions of each lensed image of JD1), with inset plots focused on each component and the spectroscopic target (henceforth JD1).

The multiband NIRCam photometry (F115W, F150W, F200W, F277W, F356W, F410M, F444W) alone confirms JD1 as a $z \approx 10$ photometric candidate. Its colours are consistent with the Lyman break residing between the F115W and F150W filters, where all photons more energetic than rest-frame Lyman-α have been absorbed and scattered by intervening intergalactic hydrogen, while the galaxy is detected at high significance at all wavelengths redward of Lyman-α (that is, the F200W, F277W, F356W, F410M and F444W filters). Combining the NIRCam data with deep Hubble Space Telescope (HST) Frontier Field photometry (including the WFC3 F160W, F140W, F125W, F105W and ACS F814W filters) from Zitrin et al.[3], a fit to the spectral energy distribution (SED) with the photometric redshift code, EAzY[4], yields a precise photometric redshift $z = 9.68^{+0.11}_{-0.10}$ (consistent with the geometric redshift predicted from lens models[3,5], $z > 8.6$ at 95% confidence level (CL)). The results of the fitting, along with the NIRCam images, are shown in the top panel of Fig. 2, and include a forced fit of a $z < 4$ interloper, for comparison (see also Extended Data Fig. 1 for a comparison of $P(z)$ constraints resulting from different subsets of the data). A $z \approx 10$ solution is clearly favoured, with a $P(z)$ governed by a dominant $z_{phot} = 9.68$ peak and a smaller, secondary peak at $z_{phot} = 2.24$, the latter of which is statistically rejected due to its increased χ^2 statistic ($\chi^2 = 46.1$ and $\chi^2 = 123.6$ for the high-z and low-z fits, respectively). The colours of images A and B are identical within the uncertainties, and from a geometric standpoint their morphologies are consistent with the expected lensing configuration, further confirming their identification as multiple images of the same source. A low redshift solution is also ruled out by the positions and comparable fluxes of the multiple images: for a $z \approx 10$ solution both images are expected to show similar offsets relative to the critical magnification line, and thus to have comparable fluxes. This contrasts with a $z = 2.24$ solution, which would place the critical line far closer to the A component (Fig. 1) and result in a different position.

The NIRSpec spectrum of the galaxy (bottom panel of Fig. 2), spanning a wavelength range $\lambda_{obs} \simeq 0.6$–5.3 μm, provides the third and conclusive piece of evidence for the redshift identification. A clear continuum break is apparent at ≈1.3 μm, with continued continuum emission redward of the break and noise (centred at ≈0 nJy) blueward of it. Identifying the break as the Lyman break, this alone places the galaxy at a redshift of $z \sim 9.75$, in excellent agreement with the photometric redshift estimated above, and deep into the heart of the cosmic dark ages when the Universe was mostly filled with neutral hydrogen[6]. Although [O III]$\lambda\lambda$4960,5008-Å emission lines are redshifted out of the NIRSpec/prism coverage, we identify a number of marginal emission lines in the rest-frame optical, most notably (but not limited to) the Balmer Hγ and Hβ lines, which are detected at central wavelengths of 46,856.0 Å and 52,482.1 Å with peak signal-to-noise (S/N) ratios of 4.9σ and 4.2σ using independent Gaussian fits, respectively. The two lines (and other marginal line emission) are discussed in the Methods section and refine the redshift of JD1 to $z_{spec} = 9.793 \pm 0.002$. As expected, strong Lyman-α is also not seen near the Lyman break, highlighting the likely consequence of damping-wing scattering by a highly neutral medium and indicating that this galaxy does not reside in a massive, ionized bubble. Adopting the upper limit on flux at the expected position of Lyman-α, the wavelength resolution and the F150W photometry as continuum, we set a 2σ upper limit on the rest-frame equivalent width (EW_0) of less than 9 Å. In similar fashion, we find $EW_0 = 50 \pm 14$ Å and $EW_0 = 68 \pm 15$ Å for Hγ and Hβ, respectively, and $EW_0 = 1$–83 Å (1–28 Å at $\lambda_{obs} < 4$ μm and 1–83 Å at $\lambda_{obs} > 4$ μm) for the rest of the NIRSpec spectrum using the best-fit continuum model presented in the Methods section and adopting wavelength widths set by the native wavelength grid. Although dust could play some role, the absence of strong lines in JD1 is likely to be due to a combination of its low overall star formation rate (SFR) (see below), its intrinsic faintness and its magnification. This is consistent with spectroscopic characterizations of Lyman-break galaxies at $z \sim 3$ (for example, Shapley et al.[7]) and both lensed and unlensed galaxies at $z > 7$ (refs. 8–10), all of which show enhanced specific SFRs compared to JD1.

We infer global galaxy properties from detailed SED fitting of the source, incorporating all of the spectroscopic and photometric constraints. Correcting for a fiducial magnification factor of $\mu = 13.1^{+0.7}_{-0.7}$ (ref. 5), the best-fit model (bottom panel of Fig. 2) paints a picture of a young (≈30 Myr), star-forming ($\log \mathrm{SFR}/M_* \, \mathrm{yr}^{-1} = -8.38$) and low stellar mass ($\log M_*/M_\odot = 7.48$) galaxy that is dust-poor ($A_V = 0.20$ mag), subsolar in metallicity ($\log Z_*/Z_\odot = -0.23$) and intrinsically compact (see Fig. 3 and analysis below). The inferred ultraviolet (UV) slope of the spectrum ($\beta = -1.90$) is blue and supports such a hypothesis, whereby the galaxy is dominated by a young, star-forming system that is beginning its chemical enrichment journey. The absolute UV magnitude of the system, $M_{UV} = -17.44$ mag, classifies the galaxy as a sub-L^* (≈0.05 L^*, adopting $M^*_{UV} = -20.6$ mag (refs. 11,12)) system and, given its extreme distance, ranks it as the faintest known source at comparable redshifts (cf. refs. 13,14; Fig. 4). As such, the galaxy luminosity is similar to that of the sources that are thought to provide the bulk of the UV photons

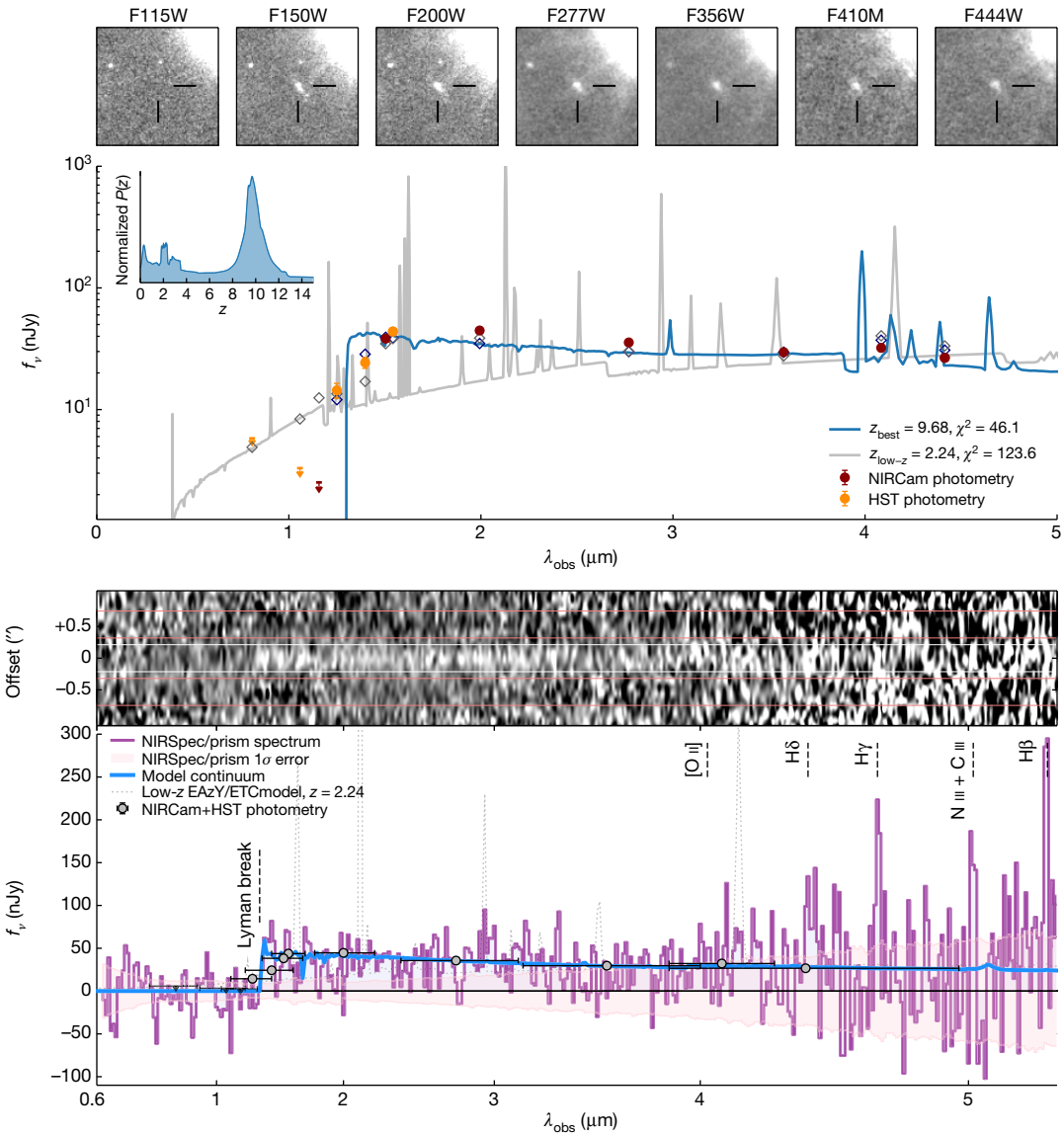

Fig. 2 | The SED and NIRSpec spectrum of JD1. Top: NIRCam postage stamp images (top panels) for each of the NIRCam bands used in this study, along with their extracted photometry (red points, and HST photometry in orange), and the best-fit SED (bottom panel, blue curve and diamonds) derived with EAzY. A forced low redshift fit is also shown (grey curve and diamonds) and is disfavoured. An inset plot highlights the $P(z)$ of the fit across the entire allowed redshift range. Bottom: the 2D (top) and 1D (bottom) NIRSpec prism spectrum of JD1, with the positive and negative 2D traces indicated by white and red lines, respectively (with widths corresponding to the 1D extraction kernel). The optimally extracted 1D spectrum is shown in purple (line and fill), with associated flux uncertainties (pink fill) and best-fit continuum model in blue. The combined NIRCam and HST photometry are shown as grey points, with associated uncertainties in black. Simulated NIRSpec spectra using the EAzY best-fit SEDs are shown as dotted grey and blue lines (low-z and high-z, respectively), for illustration. The 1D spectrum is normalized to the F150W band. All uncertainties refer to 1σ standard deviation.

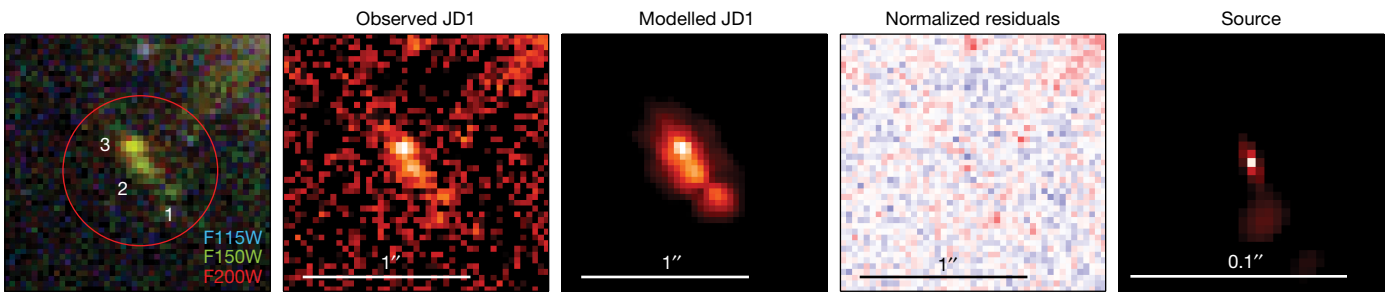

Fig. 3 | The morphology of JD1 from JWST NIRCam imaging. Left to right: an RGB (F115W, F150W, F200W) image of the galaxy system, the F150W image of the source, the lenstruction model of the source, the (1σ flux-normalized) residuals between the F150W data and the model, and the reconstructed source-plane galaxy. The sizes of the cut-outs are labelled in each panel.

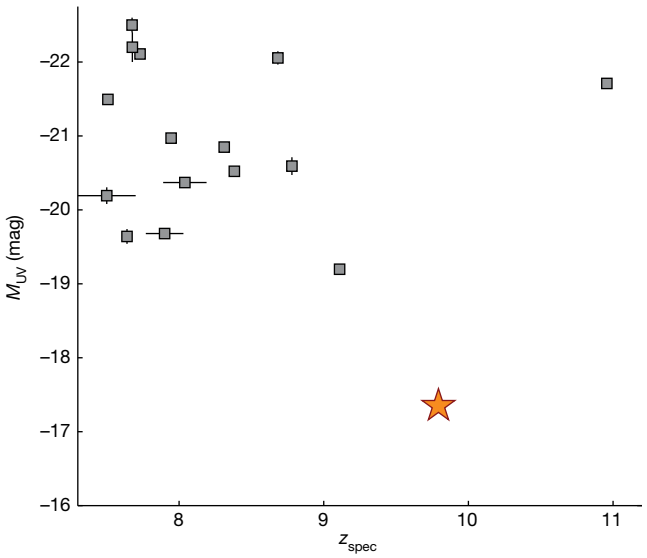

Fig. 4 | Spectroscopically confirmed sources and their absolute magnitudes. A compilation of sources in the literature[13–25] with spectroscopic redshifts (from near-infrared observations of Lyman-α or the Lyman break, or sub-mm observations of far-infrared lines such as [O III] 88 microns) and their associated M_{UV} values (grey squares), compared with JD1 (orange star). For consistency, all literature M_{UV} values are calculated using the sources' H_{160} photometry and their spectroscopic redshifts, and assuming a UV slope $\beta = -2$. JD1 is by far the lowest luminosity source (by approximately 2 mag) at comparable redshifts.

required to reionize the Universe[1,2]. We list the best-fit properties and uncertainties in the bottom half of Extended Data Table 1.

Finally, the combination of lensing magnification and JWST's extraordinary angular resolution results in an effective source-plane resolution of approximately 80 pc, allowing us to characterize the morphology of the galaxy (Fig. 3). JD1 comprises two main components: a primary knot (component 3) that likely dominates the signal in the prism spectrum, and an extended component characterized by two fainter knots (components 1 and 2). The complex morphology is also observed in individual NIRCam bands out to ≈5 μm (Fig. 2). The nucleic profiles (components 1 and 3) are well described by a Sérsic index (component 3) and a pure point spread function (PSF), whereas the more extended nature of component 2 is modelled by an exponential Sérsic profile (see details in the Methods section). The profiles yield effective radii of ≈22–40 mas for the nucleic components and 0.12″ for the extended component, which, after de-lensing along the magnification stretch of the source, translate to ≈18–30 pc and 100 ± 25 pc, respectively. Using the secure spectroscopic redshift, we adopt a forward-modelling approach with the lenstruction code and deflection maps from Bergamini et al.[5] to reconstruct JD1 in the source plane: from the NIRCam F150W image (second panel of Fig. 3), we find that an exponential Sérsic profile combined with two-dimensional (2D) shapelets provides an excellent fit to the data (third and fourth panels of Fig. 3) and results in a compact source-plane morphology with an effective radius of ≈34 pc (last panel of Fig. 3).

The combination of JD1's spectroscopic confirmation and magnification affords a unique and unprecedented insight into the physics of an ultra-faint galaxy in the cosmic dark ages, providing a first glimpse at the power of JWST and highlighting exactly what the observatory was built for. The unveiling of entire populations of faint galaxies and their physical properties through unbiased measurements now represents the logical next step and leap in our ability to characterize the sources that reionized the Universe.

Online content

Any methods, additional references, Nature Portfolio reporting summaries, source data, extended data, supplementary information, acknowledgements, peer review information; details of author contributions and competing interests; and statements of data and code availability are available at https://doi.org/10.1038/s41586-023-05994-w.

1. Robertson, B. E., Ellis, R. S., Furlanetto, S. R. & Dunlop, J. S. Cosmic reionization and early star-forming galaxies: a joint analysis of new constraints from Planck and the Hubble Space Telescope. *Astrophys. J. Lett.* **802**, L19 (2015).
2. Stark, D. P. Galaxies in the first billion years after the Big Bang. *Annu. Rev. Astron. Astrophys.* **54**, 761–803 (2016).
3. Zitrin, A. et al. A geometrically supported z~10 candidate multiply imaged by the Hubble Frontier Fields cluster A2744. *Astrophys. J. Lett.* **793**, L12 (2014).
4. Brammer, G. B., van Dokkum, P. G. & Coppi, P. EAZY: a fast, public photometric redshift code. *Astrophys. J.* **686**, 1503–1513 (2008).
5. Bergamini, P. et al. New high-precision strong lensing modeling of Abell 2744. Preparing for JWST observations. *Astron. Astrophys.* **670**, A60 (2023).
6. Mason, C. A. et al. Inferences on the timeline of reionization at z~8 from the KMOS Lens-Amplified Spectroscopic Survey. *Mon. Not. R. Astron. Soc.* **485**, 3947–3969 (2019).
7. Shapley, A. E., Steidel, C. C., Pettini, M. & Adelberger, K. L. Rest-frame ultraviolet spectra of z~3 Lyman break galaxies. *Astrophys. J.* **588**, 65–89 (2003).
8. Stark, D. P. et al. Lyα and C III] emission in z=7-9 galaxies: accelerated reionization around luminous star-forming systems? *Mon. Not. R. Astron. Soc.* **464**, 469–479 (2017).
9. Jiang, L. et al. Evidence for GN-z11 as a luminous galaxy at redshift 10.957. *Nat. Astron.* **5**, 256–261 (2021).
10. Williams, H. et al. Spectroscopy from Lyman alpha to [O III] 5007 of a triply imaged magnified galaxy at redshift z=9.5. Preprint at https://doi.org/10.48550/arXiv.2210.15699 (2022).
11. Bouwens, R. J. et al. UV luminosity functions at redshifts z~4 to z~10: 10,000 galaxies from HST Legacy Fields. *Astrophys. J.* **803**, 34 (2015).
12. Oesch, P. A., Bouwens, R. J., Illingworth, G. D., Labbé, I. & Stefanon, M. The dearth of z~10 galaxies in all HST Legacy Fields – the rapid evolution of the galaxy population in the first 500 Myr. *Astrophys. J.* **855**, 105 (2018).
13. Oesch, P. A. et al. A remarkably luminous galaxy at z=11.1 measured with Hubble Space Telescope grism spectroscopy. *Astrophys. J.* **819**, 129 (2016).
14. Hashimoto, T. et al. The onset of star formation 250 million years after the Big Bang. *Nature* **557**, 392–395 (2018).
15. Finkelstein, S. L. et al. A galaxy rapidly forming stars 700 million years after the Big Bang at redshift 7.51. *Nature* **502**, 524–527 (2013).
16. Oesch, P. A. et al. A spectroscopic redshift measurement for a luminous Lyman break galaxy at z=7.730 using Keck/MOSFIRE. *Astrophys. J. Lett.* **804**, L30 (2015).
17. Watson, D. et al. A dusty, normal galaxy in the epoch of reionization. *Nature* **519**, 327–330 (2015).
18. Zitrin, A. et al. Lymanα emission from a luminous z=8.68 galaxy: implications for galaxies as tracers of cosmic reionization. *Astrophys. J. Lett.* **810**, L12 (2015).
19. Hoag, A. et al. Spectroscopic confirmation of an ultra-faint galaxy at the epoch of reionization. *Nat. Astron.* **1**, 0091 (2017).
20. Laporte, N. et al. Dust in the reionization era: ALMA observations of a z=8.38 gravitationally lensed galaxy. *Astrophys. J. Lett.* **837**, L21 (2017).
21. Tamura, Y. et al. Detection of the far-infrared [O III] and dust emission in a galaxy at redshift 8.312: early metal enrichment in the heart of the reionization era. *Astrophys. J.* **874**, 27 (2019).
22. Bouwens, R. J. et al. Reionization Era Bright Emission Line Survey: selection and characterization of luminous interstellar medium reservoirs in the z>6.5 Universe. *Astrophys. J.* **931**, 160 (2022).
23. Laporte, N. et al. Probing cosmic dawn: ages and star formation histories of candidate $z \gtrsim 9$ galaxies. *Mon. Not. R. Astron. Soc.* **505**, 3336–3346 (2021).
24. Topping, M. W. et al. The detection of ionized carbon emission at z~8. *Astrophys. J. Lett.* **917**, L36 (2021).
25. Roberts-Borsani, G. et al. Early results from GLASS-JWST. I: confirmation of lensed $z \gtrsim 7$ Lyman-break galaxies behind the Abell 2744 cluster with NIRISS. *Astrophys. J. Lett.* **938**, L13 (2022).

Publisher's note Springer Nature remains neutral with regard to jurisdictional claims in published maps and institutional affiliations.

Springer Nature or its licensor (e.g. a society or other partner) holds exclusive rights to this article under a publishing agreement with the author(s) or other rightsholder(s); author self-archiving of the accepted manuscript version of this article is solely governed by the terms of such publishing agreement and applicable law.

© The Author(s), under exclusive licence to Springer Nature Limited 2023

Methods

Cosmological model

The cosmological parameters adopted in this paper are H_0 = 70 km s^{-1} Mpc^{-1}, Ω_m = 0.3 and Ω_Λ = 0.7. All magnitudes are quoted in the AB system[26].

JWST/NIRCam data reduction and photometry

We reduced all broadband NIRCam images (F115W, F150W, F200W, F277W, F356W and F444W) adopting the procedures and methods outlined by Merlin et al.[27]; we refer the reader to that paper for full details but provide a summary here. We used the public Space Telescope Science Institute (STScI) pipeline (v. 11.16.14) with the latest set of reference files and zero points (jwst_1023.pmap), and began the data reduction with the calwebb_detector1 and calwebb_image2 routines on the uncalibrated raw images to apply flat-field and dark current corrections, and to obtain data-quality flags that denote bad pixels or detector-level defects. Using a combination of the resulting pixel masks and a customized version of the SExtractor code[28], further custom procedures were made to the images to correct for persisting 1/*f* noise, 'snowballs' and stray light. Single exposure images were then stacked in mosaics and re-binned onto a common pixel grid using SWARP[29]. The images were aligned to Gaia DR3 data with the code SCAMP[30], using pre-existing catalogues of Magellan data. The average difference between the two astrometric solutions is of approximately 1 mas, with a normalized median absolute deviation of approximately 15 mas.

The detection image of the galaxy is the co-added F444W image, and extraction of the fluxes was performed in the same manner as in Merlin et al.[27]. In short, we used the code A-PHOT[31] to measure the fluxes within fixed circular apertures with diameter 2 × full-width at half-maximum (FWHM) of the F444W image (0.28″), on PSF-matched images; these fluxes provide robust colours, which were used to scale the total F444W flux (estimated with a Kron elliptical aperture) obtaining total fluxes in all bands. As the object is located near a bright source, it is likely contaminated by the neighbour's light; we therefore applied a local background subtraction module. We find good consistency comparing the total F150W flux with the flux given by Zitrin et al.[3] for WFC3 F160W. The resulting photometry and coordinates of JD1 are listed in the top half of Extended Data Table 1.

JWST/NIRSpec observations, data reduction and spectral extraction

JD1 is composed of three image components, two of which (components A and B in the north; Fig. 1) reside sufficiently close to each other to cause spectral overlap and a third that, while residing on the south side of the foreground cluster, appears far fainter than its counterparts. As such, we target the brightest of the three images, component B. The observations were carried out on 23 October 2022 with low-resolution ($R = \lambda/\Delta\lambda \simeq 50–350$) prism spectroscopy, adopting a three-shutter slitlet (approximately 0.2″ × 1.2″) in the micro-shutter array (MSA) and nodding pattern over a total exposure time of ≈1.23 h. The position(s) of the slit (shutters) relative to the galaxy are shown in the inset image of Fig. 1. The observations were carried out over two different pointings but with identical set-ups and position angles.

All exposures were reduced using the latest reference files (jwst_1023.pmap, including in-flight NIRSpec flats), beginning first with the calwebb_detector1 on the raw exposures to correct for detector-level artefacts and converting to count-rate images. We then used the msaexp software for the rest of the data reduction, which included preprocessing scripts to identify and correct for 1/*f* noise, 'snowballs' and bias current for each exposure and official STScI pipeline routines for the bulk of the data reduction. Those routines include AssignWcs, Extract2dStep, FlatFieldStep, PathLossStep and PhotomStep, which perform WCS registration, 2D spectral extraction, flat-fielding, pathloss corrections and both wavelength and flux calibrations on each exposure. The reduced 2D exposures were then background-subtracted using their paired exposures from the three-shutter dither and drizzled to a common grid, before being combined into a single 2D spectrum via the median of their inverse-variance-weighted exposures, including the rejection of outliers. The drizzling and stacking of the NIRSpec exposures allowed us to increase the resulting S/N of the spectrum; although this may introduce some correlation between pixels, we limited such effects by adopting a grid at the spectrum's native resolution. All exposures were visually inspected by two authors (G.R.-B. and W.C.) after each main step. One-dimensional (1D) spectra were subsequently extracted from the final 2D image using an optimal extraction procedure[32], which uses the collapsed spectrum (summed over the dispersion direction) to construct a Gaussian extraction kernel based on the spatial profile of the spectrum. The collapse of the spectrum over the full wavelength range ensures that PSF broadening is accounted for in the extraction kernel. The routine was run on the 2D flux image and on the variance image (squaring the weighting factor) to extract the spectrum and 1σ uncertainties, the latter of which also incorporates bad pixel masking. The resulting spectrum (and uncertainties) was normalized to the NIRCam/F150W photometry and is presented in the bottom panel of Fig. 2. The wavelength range covers λ_{obs} = 0.6–5.3 μm which, for a $z \approx 10$ object includes the entire rest-frame UV spectrum, while the flux calibration accuracy across the full wavelength coverage is estimated at 5% or lower (https://jwst-crds.stsci.edu/display_all_contexts/).

Photometric redshift estimates and Exposure Time Calculator simulations

We used the photometric redshift code, EAzY, to determine a precise photometric redshift using both NIRCam and HST photometry (the latter from Zitrin et al.[3]). The HST filters used (in addition to the NIRCam bands described above) were WFC3 F160W, F140W, F125W, F105W and ACS F814W. Although deep Spitzer/InfraRed Array Camera (IRAC) data also exist over the Abell 2744 cluster, the relatively poor spatial resolution makes photometry close to the cluster centre uncertain and prone to contamination. As such, we opted not to use those here. We adopted the default set of galaxy SED templates (v.1.3), which, among others, include SEDs of dusty, $z \approx 2$ star-forming galaxies and templates with strong emission lines. We allowed a redshift range of z = 0–15 (adopting a flat prior) and fitted a linear combination of the templates to the photometry. All other default settings were adopted. We ran the code on the photometry described above, in addition to two other iterations, one with HST photometry only and one with NIRCam photometry only, to assess the constraining power of each dataset in deriving a reliable photometric redshift. The resulting $P(z)$ from each of the fits are shown in Extended Data Fig. 1, where clearly photometry longward of ≈2 μm is necessary to accurately constrain the location of the Lyman break at $z > 9$ and exclude low-z solutions (we note that the photo-z analysis of Zitrin et al.[3] employed >3-μm upper limits from Spitzer/IRAC). The best-fit SED is found to confidently lie at a redshift of $z_{phot} = 9.68^{+0.11}_{-0.10}$.

For illustration purposes, we use the best-fit SEDs to simulate expected NIRSpec spectra from each, using the JWST Exposure Time Calculator (ETC) and adopting our observational set-up. The simulations are plotted as dashed grey and blue lines (for the low-z and high-z SEDs, respectively) in Fig. 2 (bottom panel) and highlight the inconsistency between our observed NIRSpec spectrum and the prominent emission lines expected from a low-z solution.

Strong lensing models

To check the robustness of our results with respect to the lens model, we used two lens models, described below. One is the recently published model by Bergamini et al.[5], and the second is a major update of the Zitrin et al.[3] model. The two models are based on a large number of observational constraints and represent the state of the art. They give mutually consistent results, so our conclusions are independent on the choice of lens model. When necessary, we use the magnification

from Bergamini et al.[5], but all the inferred numbers would be the same within the uncertainties for the other model.

In the first model, detailed by Bergamini et al.[5], the cluster total mass distribution was reconstructed using the positions of 90 multiple images from 30 different point-like sources, with spectroscopic redshifts between 1.69 and 5.73. Internal velocity dispersion measurements of 85 cluster galaxies were exploited to calibrate the subhalo mass component, which includes 225 cluster galaxies. For this work, we enhanced this model by including three additional photometric and strongly lensed sources identified with the recently acquired JWST/Near-InfraRed Imager and Slitless Spectrograph (NIRISS) data with a total of eight multiple images, including two (A and B) of JD1. We also updated the positions of all the mass components and multiple images in the lens model, adopting the new JWST astrometric grid. The total root mean square (r.m.s.) separation between the observed and model-predicted positions is 0.37 arcsec (the same as in the original model[5]). To estimate the median magnification values and the CL intervals, we extracted 500 random sets of parameter values from the final Markov chain Monte Carlo (MCMC) chain, which has a total of 2.5×10^6 samples. The predicted magnification values, with their 1σ confidence level statistical uncertainties, are $\mu_A = 12.0^{+1.0}_{-0.9}$ and $\mu_B = 13.1^{+0.7}_{-0.7}$ for the multiple images A and B, respectively. The magnification ratio is in excellent agreement with the photometric measurements of images A and B. The redshift value of JD1 predicted by this strong lensing model is $z_{lens} > 8.6$ at the 95% CL, assuming a uniform prior between $z = 2$ and $z = 12$, thereby fully consistent with the spectroscopic and photometric redshifts of image B.

The second lens model used here is an update to the model for Abell 2744 presented by Zitrin et al.[3], revisited here as follows. As input we started with the list of cluster members, and multiple image systems from Bergamini et al.[5], which are based on recent spectroscopic measurements from the Very Large Telescope's Multi Unit Spectroscopic Explorer (MUSE) instrument. Following Bergamini et al.[5], external mass clumps around the main central cluster core are also included in this update. However, we limited the external clump positions to places where strong lensing supports them, that is, we identified a few potential multiply-imaged systems in the northern part of the cluster, and used them to improve the part of the model for which only weak lensing measurements have thus far been available. Furthermore, as our goal was to estimate properties of the high-redshift source images, we also included images A and B as constraints. We built our updated model with a revised, analytic version of the parametric method used by Zitrin et al.[33] to model the Cluster Lensing And Supernova survey with Hubble (CLASH) sample. The main update is that the new version is not coupled to a specific grid resolution, and thus can achieve more accurate results. Similar to other parametric methods, the model assumes two main components: a superposition of all clusters members, parametrized each here as double pseudo-isothermal elliptical density profiles, based on common scaling relations[34]; and a dark matter component consisting of larger-scale halos, parametrized here as pseudo-isothermal elliptical mass distributions. In addition, the model can accommodate external shear, if warranted by the data. In addition to the mass associated with the luminous galaxies, we distribute five dark matter halos: two halos are centred on the two central bright galaxies, but their central position is free to move; the other three are fixed to the three bright galaxies in the northern part of the field, about 2.5 arcminutes northwest of the main clump, seen in extended images of the field (for example, ref. 35). Following common practice, we adopted a scaling relation to connect the galaxies to their dark matter halos. We left as free parameters the velocity dispersion and cut-off radius of a L^* galaxy, and the exponents of the relations themselves. For all dark matter halos, the velocity dispersion, core radius, ellipticity and position angle were free to be optimized. We also left free the velocity dispersion of six bright galaxies in the central part, and the ellipticity parameters of the brightest cluster galaxy. The minimization is done in the source plane, via an MCMC procedure. We obtain an r.m.s. value of $\simeq 0.6$ arcsec. We obtain magnification estimates of 10.7 ± 0.6, 11.9 ± 0.8 and 3.1 ± 0.2 for images A, B and C, respectively, consistent with the ones obtained by Bergamini et al.[5]. Further details of the model will be given by L.J.F. et al. (manuscript in preparation).

Spectrophotometric modelling and analyses

We conducted a SED-fitting analysis by using a publicly available code, gsf, which allowed us to fit both photometric and spectroscopic data simultaneously[36]. The code generates model templates by using fsps[37] with the initial mass function set to the parameters of ref. 38. We assume a Small Magellanic Cloud dust attenuation curve[39]. The spectral templates are matched to the resolution of the observed spectrum, $R \approx 100$, for spectral data, whereas broadband data points are fitted with the model photometry after convolving the templates by the corresponding filters. We adopted a non-parametric form for star formation histories by following the method presented in Morishita et al.[36]. For the redshift of JD1, we generated multiple templates of different ages (1, 3, 10, 30, 100 and 300 Myr). An emission line component of ionization parameters $\log U \in [-3{:}0]$, also generated by fsps, was added by the amount of an amplitude parameter. Dust attenuation, metallicity of the stellar templates and redshift were left as free parameters. In sum, we had $6 + 2 + 1 + 1 + 1 = 11$ free parameters. The posterior distribution of the parameters was sampled by using emcee[40] for 10^5 iterations with the number of walkers set to 100. The final posterior was collected after excluding the first half of the realizations (known as burn-in). The resulting best-fit continuum model is shown in Fig. 2 (bottom panel); the physical parameters quoted in the main text and tabulated in Extended Data Table 1 are the 50th percentile of the posterior distribution, along with the 16th to 84th percentile uncertainty ranges. The SFR is calculated as the average of the posterior star formation history over the last 100 Myr.

Source morphology

JD1 shows a clear elongated shape along the magnification stretch in which three main components are identified (two nucleated, labelled 1 and 3, and one extended, labelled 2, as shown in Fig. 3). The morphology of the system is analysed by exploiting the JWST/NIRCam images presented here. As performed in Vanzella et al.[41], we ran GALFIT[42] to reproduce the observed JD1 image in the NIRCam/F150W band. This band offers the sharpest PSF while probing pure stellar continuum not affected by Lyman-α emission (if any) and the attenuation from the intergalactic medium. The underlying extended component (2) is modelled by adopting a Sérsic light profile ($n = 4$), effective radius of 4 pixels, a position angle of 53° and an axis ratio (b/a) of 0.2. The nucleated emissions were modelled adopting a pure PSF for component 1 and a Sérsic ($n = 1$) model for component 3. Very similar results are obtained adopting Gaussian ($n = 0.5$), exponential ($n = 1$) or $n = 4$ indexes, for both the nucleated (when applying a Sérsic model) and the extended components. Specifically, the pure PSF model of component 1 corresponds to an upper limit on the radius, which can be associated to the half width at half maximum of the PSF ($\simeq$40 mas, in the observed plane, in the F150W image). The brighter component 3 is well reproduced with a Sérsic model and effective radius of $\approx$22 mas (approximately 0.7 pixels). The extended component is less constrained, however, with an effective radius of 0.12″ (observed). After de-lensing along the magnification stretch (adopting $\mu_{tang} = 5.2$; ref. 5), such angular scales translate to an upper limit of 30 pc for the compact component 1, of order 18^{+8}_{-5} pc for component 3 and 100 ± 25 pc for the extended one (component 2). However, it is worth stressing that the size of the elongated component can be underestimated because of the faintness of the system.

We further performed a source reconstruction of JD1 in the source plane, by following the procedure outlined by Yang et al.[43], using the lenstruction lensing code and a forward-modelling approach. Again using the F150W image, the parametrization of JD1 in the source plane

was done using an elliptical Sérsic profile to describe the central knot (which likely dominates the NIRSpec spectrum) and 2D shapelets to describe the extended and irregular component. The light profile is then subjected to the deflection maps of the Bergamini et al.[5] lens model and convolved to the F150W PSF to mimic lensing effects and match the surface brightness of JD1. The F150W data and results of the modelling are shown in the second and third panels of Fig. 3, where we find an excellent fit to the data by the model, as seen by the normalized residuals between the two (normalized by the 1σ data uncertainties; see the fourth panel of Fig. 3). The source-plane model of JD1 (last panel) is found to be very compact, with a half-light radius of approximately 34 pc.

Identification of marginal emission lines and flux limits

We observe flux peaks in both the 1D and 2D spectra that stand out from local fluctuations, at observed wavelengths of approximately 4.68 μm and 5.25 μm. Using the redshift of the Lyman break, the rest-frame wavelengths fall on the expected positions of Hγ and Hβ. We inspect the individual exposures of the NIRSpec spectrum as well as a variety of extraction profile widths Methods to ensure the putative lines are not a result of artefacts (for example, snowballs, cosmic ray hits or the width of the extraction profile). We see no evidence to suggest they may be and note they are seen only in the combined spectrum, as expected given their flux. We fitted the two lines with simple Gaussian profiles using emcee[40]. Using the peaks of the fits and the standard deviation of the local flux immediately adjacent to the lines, we measured peak S/N ratios of 4.9σ and 4.2σ for the putative Hγ and Hβ lines. The integrated line ratio of the two is Hγ/Hβ = 0.81 ± 0.38, consistent within uncertainties with ratios reported in the literature for Sloan Digital Sky Survey (SDSS) galaxies (0.458–0.475; ref. 44). The central wavelengths place them at z = 9.792 ± 0.004 and z = 9.793 ± 0.001 (for Hδ and Hβ, respectively), in near-perfect agreement with the independent redshift measurement from the Lyman break ($\delta z \simeq 0.043$), thus refining the redshift of JD1 to z_{spec} = 9.793 ± 0.002 (taken as the mean redshift of the two lines). Assuming Gaussian probabilities, we find the detection of both of these lines at their significance and at coincidental redshifts to be a 6.6σ event. We note that, at a redshift of z_{spec} = 9.793, strong [O III]$\lambda\lambda$4960,5008-Å emission lines are redshifted out of the NIRSpec/prism coverage.

Additionally, the spectrum also shows a prominent peak at approximately 5.01 μm, in perfect agreement with the redshift given by the Balmer lines, and which coincides with the locations of the N III$\lambda\lambda\lambda$4634,4640,4641 Å and C III$\lambda\lambda\lambda$4647,4650,4651 Å triplets. The line profile (measured as a single Gaussian fit given the low spectral resolution and proximity of the lines between themselves) is sufficiently broad to encompass both triplets, and is thus likely to be the result of the combined contribution from those six lines. Using our best-fit continuum model, we measure EW$_0$ = 78 ± 19 Å. Although such lines are not common among the general galaxy population, their origin derives from dense and energetic stellar winds ejected by massive Wolf–Rayet (WR) stars. Although WR galaxies are comparatively rare among the general population, they have been found in their hundreds at low redshift from rest-frame optical studies with, for example, the SDSS, Calar Alto Legacy Integral Field Area Survey (CALIFA) and Mapping Nearby Galaxies at Apache Point Observatory (MaNGA) surveys (for example, refs. 45–47). The absence of significant flux at the locations of more highly ionized N IV$\lambda\lambda\lambda$3479,3484,4058-Å and N IV$\lambda\lambda$4603,4619-Å lines would indicate WR stars of type WN8h–WN9h, characterized by stellar masses, radii and effective temperatures of ≳30 $M_\odot$, ≳20 $R_\odot$ and approximately 35,000–40,000 K (ref. 48).

The spectrum of WN8h–WN9h WR stars is also dominated by low ambient metallicity, which could explain (together with the lower spectral resolution at bluer wavelengths) the apparent absence of the [O II]$\lambda\lambda$3726,3729-Å doublet (EW$_0$ < 26 Å, at 2σ) and lead to significantly weaker stellar winds that reduce the line widths of the profiles[49,50]. With an ionization potential effectively double that of the above triplets (that is, 54.4 eV cf. 29.6 eV and 24.4 eV, respectively), He IIλ4685 Å requires extreme radiation fields more commonly associated with active galactic nuclei[51]. As such, its apparent absence (EW$_0$ < 12 Å, at 2σ), and the absence of other high ionization lines in the rest-frame UV, is unsurprising and supports the hypothesis of a metal-poor system without extreme radiation fields from active galactic nuclei. As such, one hypothesis is that the gravitational amplification and stretching of JD1's image (Figs. 1 and 3) provides—together with the position of the NIRSpec slit—a unique viewpoint into a source-plane region of the galaxy where the light is dominated by a population of these massive stars rather than the integrated light dominated by massive OB stars.

No other comparable flux peaks (positive or negative) are seen in the 1D spectrum of JD1. Although there are a very small number of similar peaks in the red (>4 μm) portion of the 2D spectrum outside the kernel trace, no other such examples show multiple peaks that simultaneously (1) fall at redshifts coinciding with the Lyman break and (2) show similar spatial extent to JD1's continuum profile. The detection of the three lines discussed above at their measured significance and at coincidental redshifts is found to be a 7.6σ event. Nevertheless, we consider only the marginal Balmer lines sufficiently detected for a minor refining of the galaxy redshift, and ultimately both deeper and higher resolution data will be required to verify the presence and origin of all the tentative emission lines reported here.

Data availability

All data used in this paper are publicly available through the Mikulski Archive for Space Telescopes (MAST) server with the relevant program IDs (2561 for the NIRCam imaging, 2756 for the NIRSpec spectroscopy). All other data generated throughout the analysis are available from the corresponding author on request or at https://github.com/guidorb/jwst-nirspec-jd1.Source data are provided with this paper.

Code availability

Our analysis makes use of three primary codes, all of which are publicly available. The photometric redshift analyses were performed with EAzY, the latest version of which (including the templates used here) is available at https://eazy-py.readthedocs.io/en/latest/. The data reduction of the NIRCam images were performed with the official STScI JWST pipeline, which can be found here: https://github.com/spacetelescope/jwst. The NIRSpec data were reduced using the msaexp code, which can be found here: https://github.com/gbrammer/msaexp. The reduced NIRSpec spectrum was analysed with the gsf code, which is available here: https://github.com/mtakahiro/gsf. The morphological source-plane reconstruction was done with lenstruction, found here: https://github.com/ylilan/lenstruction.

26. Oke, J. B. & Gunn, J. E. Secondary standard stars for absolute spectrophotometry. *Astrophys. J.* **266**, 713–717 (1983).
27. Merlin, E. et al. Early results from GLASS-JWST. II. NIRCam extragalactic imaging and photometric catalog. *Astrophys. J. Lett.* **938**, L14 (2022).
28. Bertin, E. & Arnouts, S. SExtractor: software for source extraction. *Astron. Astrophys. Suppl.* **117**, 393–404 (1996).
29. Bertin, E. SWarp: resampling and co-adding FITS images together. *Astrophysics Source Code Library* record ascl:1010.068 (2010).
30. Bertin, E. Automatic astrometric and photometric calibration with SCAMP. In *Astronomical Data Analysis Software and Systems XV, Vol. 351 of Astronomical Society of the Pacific Conference Series* (eds Gabriel. C. et al.) 112–115 (2006).
31. Merlin, E. et al. A-PHOT: a new, versatile code for precision aperture photometry. *Astron. Astrophys.* **622**, A169 (2019).
32. Horne, K. An optimal extraction algorithm for CCD spectroscopy. *Publ. Astron. Soc. Pac.* **98**, 609–617 (1986).
33. Zitrin, A. et al. Hubble Space Telescope combined strong and weak lensing analysis of the CLASH sample: mass and magnification models and systematic uncertainties. *Astrophys. J.* **801**, 44 (2015).
34. Jullo, E. et al. A Bayesian approach to strong lensing modelling of galaxy clusters. *New J. Phys.* **9**, 447 (2007).
35. Merten, J. et al. Creation of cosmic structure in the complex galaxy cluster merger Abell 2744. *Mon. Not. R. Astron. Soc.* **417**, 333–347 (2011).

36. Morishita, T. et al. Massive dead galaxies at $z\sim2$ with HST grism spectroscopy. I. Star formation histories and metallicity enrichment. *Astrophys. J.* **877**, 141 (2019).
37. Conroy, C., Gunn, J. E. & White, M. The propagation of uncertainties in stellar population synthesis modeling. I. The relevance of uncertain aspects of stellar evolution and the initial mass function to the derived physical properties of galaxies. *Astrophys. J.* **699**, 486–506 (2009).
38. Chabrier, G. Galactic stellar and substellar initial mass function. *Publ. Astron. Soc. Pac.* **115**, 763–795 (2003).
39. Gordon, K. D., Clayton, G. C., Misselt, K. A., Landolt, A. U. & Wolff, M. J. A quantitative comparison of the Small Magellanic Cloud, Large Magellanic Cloud, and Milky Way ultraviolet to near-infrared extinction curves. *Astrophys. J.* **594**, 279–293 (2003).
40. Foreman-Mackey, D., Hogg, D. W., Lang, D. & Goodman, J. emcee: the MCMC Hammer. *Publ. Astron. Soc. Pac.* **125**, 306 (2013).
41. Vanzella, E. et al. Early results from GLASS-JWST. VII: evidence for lensed, gravitationally bound proto-globular clusters at $z=4$ in the Hubble Frontier Field A2744. *Astrophys. J. Lett.* **940**, L53 (2022).
42. Peng, C. Y., Ho, L. C., Impey, C. D. & Rix, H.-W. Detailed decomposition of galaxy images. II. Beyond axisymmetric models. *Astron. J.* **139**, 2097–2129 (2010).
43. Yang, L., Birrer, S. & Treu, T. A versatile tool for cluster lensing source reconstruction - I. Methodology and illustration on sources in the Hubble Frontier Field Cluster MACS J0717.5+3745. *Mon. Not. R. Astron. Soc.* **496**, 2648–2662 (2020).
44. Groves, B., Brinchmann, J. & Walcher, C. J. The Balmer decrement of Sloan Digital Sky Survey galaxies. *Mon. Not. R. Astron. Soc.* **419**, 1402–1412 (2012).
45. Brinchmann, J., Kunth, D. & Durret, F. Galaxies with Wolf–Rayet signatures in the low-redshift Universe. A survey using the Sloan Digital Sky Survey. *Astron. Astrophys.* **485**, 657 (2008).
46. Miralles-Caballero, D. et al. First survey of Wolf–Rayet star populations over the full extension of nearby galaxies observed with CALIFA. *Astron. Astrophys.* **592**, A105 (2016).
47. Liang, F.-H. et al. Wolf–Rayet Galaxies in SDSS-IV MaNGA. I. Catalog construction and sample properties. *Astrophys. J.* **896**, 121 (2020).
48. Crowther, P. A. Physical properties of Wolf–Rayet stars. *Annu. Rev. Astron. Astrophys.* **45**, 177 (2007).
49. Crowther, P. A. & Hadfield, L. J. Reduced Wolf–Rayet line luminosities at low metallicity. *Astron. Astrophys.* **449**, 711 (2006).
50. Crowther, P. A. Observed metallicity dependence of winds from WR stars. *Stellar Evolution at Low Metallicity: Mass Loss, Explosions, Cosmology ASP Conference Series* **353**, 157 (2006).
51. Feltre, A., Charlot, S. & Gutkin, J. Nuclear activity versus star formation: emission-line diagnostics at ultraviolet and optical wavelengths. *Mon. Not. R. Astron. Soc.* **456**, 3354 (2016).

Acknowledgements G.R.-B. thanks N. Laporte for valuable conversations regarding the NIRSpec spectrum of the source. This work is based on observations made with the NASA/ESA/CSA JWST. The data were obtained from the Mikulski Archive for Space Telescopes at the Space Telescope Science Institute, which is operated by the Association of Universities for Research in Astronomy, Inc., under NASA contract NAS 5-03127 for JWST. These observations are associated with programme JWST-ERS-1324. We acknowledge financial support from NASA through grant JWST-ERS-1324. A.A., A.M., P.B., C.G., P.R. and E.V. acknowledge financial support through grants PRIN-MIUR 2017WSCC32 and 2020SKSTHZ. A.A. has received funding from the European Union's Horizon 2020 research and innovation programme under the Marie Sklodowska-Curie grant agreement no. 101024195 - ROSEAU. A.Z. and L.J.F. acknowledge support by grant no. 2020750 from the United States–Israel Binational Science Foundation and grant no. 2109066 from the United States National Science Foundation, and by the Ministry of Science & Technology, Israel. C.M. acknowledges support by the VILLUM FONDEN under grant 37459. The Cosmic Dawn Center (DAWN) is funded by the Danish National Research Foundation under grant DNRF140. B.M. acknowledges support from an Australian Government Research Training Programme Scholarship. This research is supported in part by the Australian Research Council Centre of Excellence for All Sky Astrophysics in 3 Dimensions (ASTRO 3D), through project number CE170100013. J.M.D. acknowledges the support of projects PGC2018-101814-B-100 and MDM-2017-0765. A.V.F. is grateful for support from the Christopher R. Redlich Fund and numerous individual donors. X.W. is supported by the Chinese Academy for Sciences Project for Young Scientists in Basic Research, grant no. YSBR-062. M.B. acknowledges support from the Slovenian Research Agency ARRS through grant N1-0238. R.A.W. acknowledges support from NASA JWST Interdisciplinary Scientist grants NAG5-12460, NNX14AN10G and 80NSSC18K0200 from GSFC. We acknowledge support from the Istituto Nazionale di Astrofisica (INAF) (Italian National Institute for Astrophysics) Large Grant 2022 'Extragalactic Surveys with JWST' (PI Pentericci).

Author contributions G.R.-B. led the NIRSpec data reduction and analysis with input from several co-authors. G.R.-B. and T.T. wrote the paper and developed the main interpretation of the results. A.F., M.C., E.M. and D.P. reduced the NIRCam images and provided the photometry. T.M. performed the spectral fitting and derived the physical parameters. A.A., C.G., P.B. and P.R. developed and updated the reference lens model providing predictions on lensed quantities. A.M. contributed to the construction of the photometric and spectroscopic catalogues for the lens model. A.Z. and L.J.F. constructed the new lens model and wrote the accompanying text. T.N., K.G. and W.C. assisted with NIRSpec data reduction and performed quality checks on the 1D and 2D spectra. E.V., P.R. and L.Y. performed the analysis of the source morphology. All authors discussed the results and commented on the manuscript.

Competing interests The authors declare no competing interests.

Additional information

Supplementary information The online version contains supplementary material available at https://doi.org/10.1038/s41586-023-05994-w.

Correspondence and requests for materials should be addressed to Guido Roberts-Borsani.

Peer review information *Nature* thanks Masami Ouchi and the other, anonymous, reviewer(s) for their contribution to the peer review of this work. Peer reviewer reports are available.

Reprints and permissions information is available at http://www.nature.com/reprints.

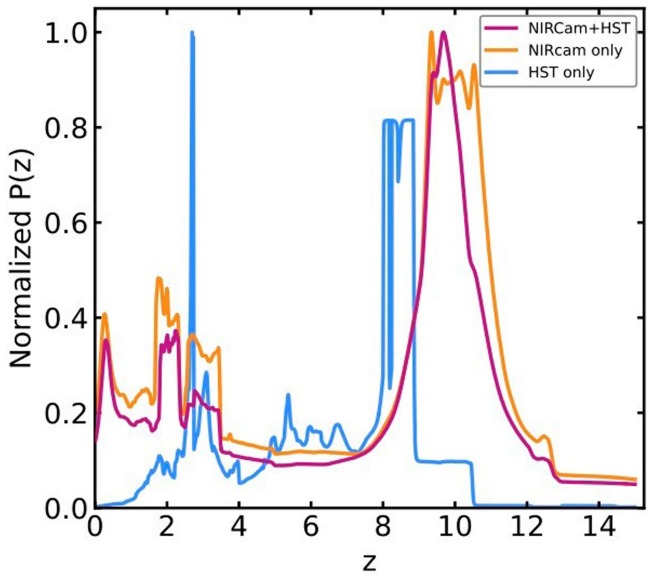

Extended Data Fig. 1 | The *P*(*z*) of JD1 from EAzY fits to a variety of photometry. Each *P*(*z*) is constructed through EAzY modelling of three sets of photometric data points. Blue adopts HST photometry only[3], orange adopts NIRCam photometry only, and red illustrates results for the combined dataset. The HST photometry provides excellent constraining power blueward of the *J*-band, but lacks the wavelength coverage in the IR that NIRCam provides to exclude low-*z* interlopers. As such, even using NIRCam data alone provides far better constraints for $z > 9$ selections. NB: The photo-*z* estimated by ref. 3 also incorporates Spitzer/IRAC photometry, not used here.

Extended Data Table 1 | Summary of the NIRCam photometry and the best-fit global properties of JD1

Property	Value
RA (J2000) [deg]	3.5950014
Dec (J2000) [deg]	-30.4007411
μ	$13.1^{+0.6}_{-0.7}$
F115W [AB]	<29.79 (2σ)
F150W [AB]	27.44 ± 0.05
F200W [AB]	27.28 ± 0.04
F277W [AB]	27.52 ± 0.04
F356W [AB]	27.72 ± 0.04
F410M [AB]	27.63 ± 0.07
F444W [AB]	27.84 ± 0.06
$z_{\rm EAzY}$	$9.68^{+0.11}_{-0.10}$
$z_{\rm spec}$	9.793 ± 0.002
$\log M_*$ [$M_\odot$]	$7.19^{+0.17}_{-0.12}$
$\log Z_*$ [$Z_\odot$]	$-0.20^{+0.14}_{-0.50}$
$\log T_*$ [Gyr]	$-1.87^{+0.77}_{-0.53}$
$A_{\rm V}$ [mag]	$0.55^{+0.11}_{-0.06}$
$\log$ SFR [M_*/yr]	$-1.14^{+0.14}_{-0.10}$
$\beta_{\rm UV}$	$-2.22^{+0.03}_{-0.02}$
$M_{\rm UV}$	$-17.35^{+0.03}_{-0.03}$

Top: a summary of the NIRCam photometry and EAzY redshift of JD1. All fluxes are uncorrected for magnification, and the fiducial magnification factor is from ref. 5. Bottom: the best-fit global properties of JD1. The properties derive from the SED analysis presented in the Methods section. All values are corrected for magnification where needed. All uncertainties refer to 1σ standard deviation unless stated otherwise.